

Electrically Tunable PN Diodes in a Monolayer Dichalcogenide

Britton W. H. Baugher*, Hugh O. H. Churchill*, Yafang Yafang, and Pablo Jarillo-Herrero

Department of Physics, Massachusetts Institute of Technology, Cambridge, MA 02139, USA

One of the most fundamental and useful devices for electronics and optoelectronics is the PN junction, which provides the functional element of diodes, bipolar transistors, photodetectors, LEDs, and solar cells, among many other devices. In conventional PN junctions, the adjacent p- and n-type regions of a semiconductor are formed by chemical doping. Materials with ambipolar conductance, however, allow for PN junctions to be configured and modified by electrostatic gating. This electrical control enables a single device to have multiple functionalities. For example, a device with two gates can operate as either an ambipolar field-effect transistor or a PN diode, depending on the settings of the gates. Here we report ambipolar monolayer WSe_2 devices in which two local gates are used to define a PN junction exclusively within the sheet of WSe_2 . With these electrically tunable PN junctions, we demonstrate both PN and NP diodes with ideality factors better than 2. Under excitation with light, the diodes show a peak photodetection responsivity of 200 mA/W and photovoltaic power generation with an external quantum efficiency of 0.2%, promising numbers for a nearly transparent monolayer sheet in a lateral device geometry. Finally, we demonstrate a light-emitting diode based on monolayer WSe_2 . These devices demonstrate a fundamental building block for ubiquitous, ultra-thin, flexible, and nearly transparent optoelectronic and electronic applications based on ambipolar dichalcogenide materials.

Next generation photodetectors and photovoltaic devices, as well as sensors, displays, and light emitting diodes, will all require new optoelectronic materials with superior characteristics to those currently in use. Candidate materials must be flexible for wearable devices, transparent for interactive displays, efficient for solar cells, and robust and low cost for broad distribution. Monolayer semiconducting transition metal dichalcogenides (TMDs) such as tungsten diselenide (WSe_2) are flexible¹, nearly transparent^{2,3}, high strength¹, direct band gap² materials that have the potential to meet all of these criteria. Tungsten diselenide's crystal structure is comprised of stacks of trilayer sheets made of a single atomic layer of tungsten encapsulated by two layers of selenium.

* These authors contributed equally to this work.

This structure leads to very strong intralayer bonding in the trilayer plane and weak interlayer bonding out of the plane. Such bonding allows for the exfoliation of bulk crystals down to a single molecular layer of Se-W-Se in a manner similar to graphene⁴.

Monolayer WSe₂ is a direct gap semiconductor with a band gap of ~ 1.65 eV (ref. 5), a complement to other two-dimensional materials such as graphene, a gapless semimetal, and boron nitride, an insulator⁶. The direct band gap distinguishes monolayer WSe₂ from its bulk and bilayer counterparts, which are both indirect gap materials with smaller band gaps^{5,7,8}. This sizable direct band gap in a two-dimensional layered material enables a host of new optical and electronic devices for both applications and fundamental investigation. Thin film TMDs have already demonstrated novel nanoelectronic and optoelectronic devices such as ambipolar and high quality field effect transistors⁹⁻¹¹, electric double-layer transistors¹², integrated circuits¹³, and phototransistors¹⁴ with high responsivity¹⁵. In addition, photoluminescence^{2,16} and electroluminescence^{17,18} have been used to observe effects such as giant spin-valley coupling¹⁹ and optical control of valley polarization^{20,21} and coherence²².

PN junctions in TMDs have, to date, been much less explored than field effect transistors. Junctions of p- and n-doped bulk WSe₂ were reported over 30 years ago²³. But only in the last few years have thin film TMDs been made into various types of PN devices, such as an ionic-liquid gated bulk MoS₂ device¹², an InAs - bulk WSe₂ heterojunction³, and a doped silicon-monolayer MoS₂ heterojunction¹⁸. Unfortunately, bulk TMDs and heterostructures involving other materials lack many of the most appealing properties of monolayer TMDs: a direct band gap, flexibility, and transparency. Here we present measurements of monolayer WSe₂ PN junctions defined and controlled by electrostatic gates. We demonstrate PN junction devices with diverse functionality, including current rectifying diodes, a photodetector, a photovoltaic device, and a light-emitting diode, and we characterize their performance.

Device fabrication begins with exfoliation of bulk, mined WSe₂ (Nanosurf Inc.) down to few-layered sheets using the mechanical cleavage method pioneered for graphene⁴. The thin flakes are deposited onto an MMA-PDMS transfer slide as described in graphene-boron-nitride device fabrication^{24,25}, and single molecular layers were identified by optical contrast²⁶ and confirmed with AFM (see Supplementary Information). These monolayers are then transferred onto a pair of split gates insulated by 20 nm of HfO₂ (grown by atomic layer deposition). The gates are separated by a 100 nm gap, patterned using e-beam lithography on a highly doped Si substrate covered in 285

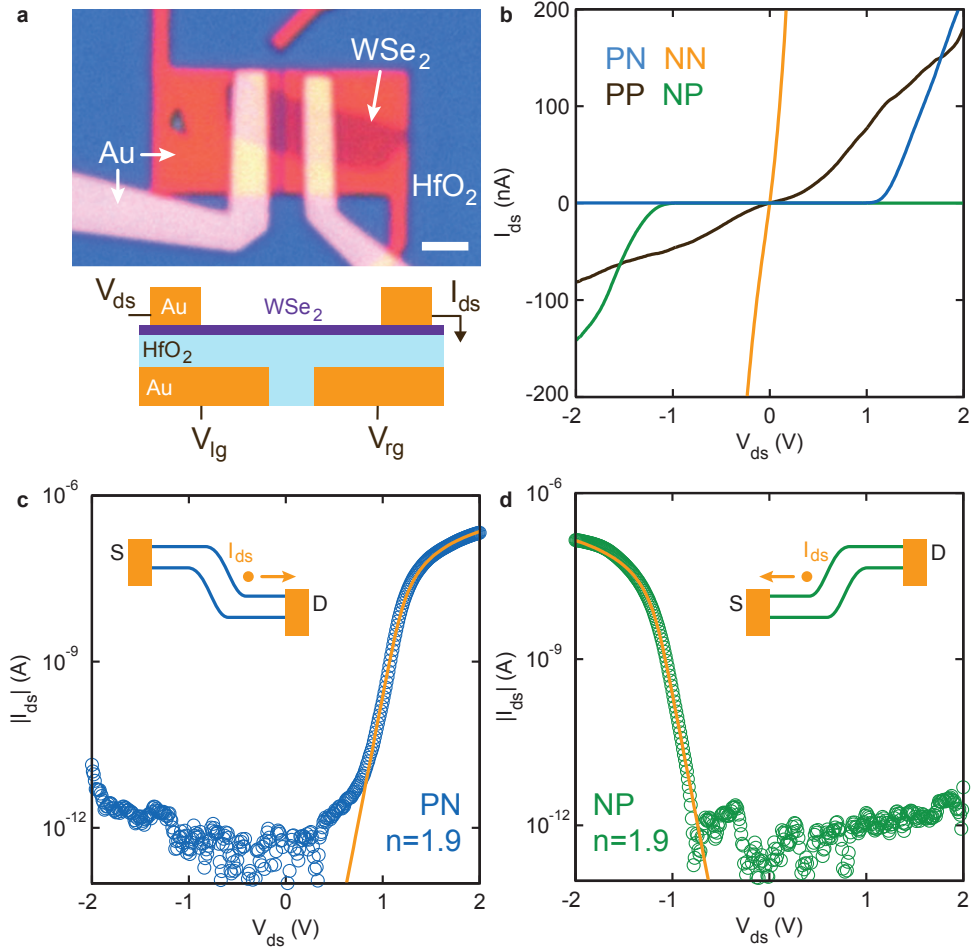


FIG. 1: **Gate-controlled monolayer WSe₂ PN junction diodes.** **a**, Optical micrograph of a monolayer WSe₂ device controlled by two local gates. The WSe₂ is contacted with Au electrodes. The flake and contacts are insulated from the gates by 20 nm of HfO₂. The scale bar is 2 μ m. Below is a schematic side view of the device including electrical connections. **b**, Current-voltage (I_{ds} - V_{ds}) curves showing transport characteristics of the four doping configurations of the device, NN, PP, PN, and NP. Both gates were set to 10 V for the NN configuration and -10 V for PP. V_{lg} was set to ± 10 V and V_{rg} to ∓ 10 V for PN/NP. The PP and NN configurations (black and yellow curves respectively) are Ohmic at low V_{ds} , while the PN and NP diodes (blue and green curves, respectively) strongly rectify current in opposite directions. **c**, **d** Semi-log plots of I_{ds} through the PN (blue circles) and NP (green circles) diodes as a function of V_{ds} with fits in yellow (see text). The fits give a diode ideality of $n = 1.9$ for both the PN and NP configurations. Insets: Diagrams of the energy levels of the device in forward bias for PN and NP configurations.

nm of thermally grown SiO₂. They are made from e-beam evaporated gold and are 20 nm thick. The WSe₂ is contacted by two gold electrodes, each approximately 1 μm wide and 25 nm thick with a 0.3 nm chromium sticking layer. An optical image of device D1 and schematic is shown in Fig. 1a.

For all transport measurements we report, a voltage bias, V_{ds} , is applied to the source contact and the DC current through the device, I_{ds} , is measured at the drain. The two back gates are capacitively coupled to the device through the HfO₂ dielectric, which has a dielectric constant, $\epsilon_r \approx 15$. All measurements were performed in vacuum ($\sim 10^{-5}$ Torr) and at room temperature.

The voltages on the two gates, V_{lg} for the left gate and V_{rg} for the right gate, independently control the carrier density in the left and right sides of the monolayer. In this way the device can be electrostatically doped into various conducting regimes (Fig. 1). With both gates grounded, the device is an insulator, indicating a low level of extrinsic doping of this natural WSe₂, in contrast with the high level of n-doping frequently observed in natural MoS₂ (ref. 4). This intrinsic property of natural WSe₂ allows ambipolar conduction, a crucial element of the operation of our devices. By adjusting the voltages on both gates together, the device can be operated as an ambipolar field-effect transistor. With both sides of the device n-doped ($V_{lg} = V_{rg} = 10$ V, denoted NN) or both sides p-doped ($V_{lg} = V_{rg} = -10$ V, denoted PP), the device shows an Ohmic current-voltage relation at low V_{ds} (Fig. 1b). The device has a significantly higher conductance in the NN configuration, most likely due to lower contact resistance between the gold and the WSe₂. We have found that gold makes better n-type than p-type contact to monolayer WSe₂, as has been observed in MoS₂ (ref. 27).

By oppositely biasing the two gates, doping one side with electrons and the other with holes, the device can rectify the flow of current as a diode. Current measurements for the two diode configurations ($V_{lg} = -10$ V, $V_{rg} = 10$ V, denoted PN and $V_{lg} = 10$ V, $V_{rg} = -10$ V, denoted NP) are shown in Fig. 1b. The same data is plotted on a semilog scale in Figs. 1c and 1d. By selecting the PN or NP configuration, the device can rectify current flowing in either direction. The drain-source currents of the PN and NP diodes are fit to an extension²⁸ of the Shockley diode equation²⁹ that includes a series resistance, R_s :

$$I_{ds} = \frac{nV_T}{R_s} W \left[\frac{I_0 R_s}{nV_T} \exp \left(\frac{V + I_0 R_s}{nV_T} \right) \right] - I_0$$

where $V_T = k_B T / q$ is the thermal voltage at a temperature T . k_B is the Boltzmann constant, and

q is the electron charge. I_0 is the reverse bias current, and n is the diode ideality factor, where $n = 1$ denotes an ideal diode. The W function is the Lambert W function.³⁰

The fits (yellow curves, Figs. 1c and 1d) give ideality factors of $n = 1.9$ for both the PN and NP configurations, indicating that the current is mostly limited by recombination rather than diffusion²⁹. The series resistances extracted from the fits are $R_s = 3M\Omega$ for PN and $R_s = 5M\Omega$ for NP. We note that our data do not strongly constrain the value of the reverse bias saturation current because it is below the 0.1 pA noise floor of our measurements. The PN and NP diodes have rectification factors of 10^5 and low reverse bias currents less than 0.1 pA, which are promising characteristics for low power electronics.

A more complete view of transport through the device is shown in a map of current as a function of the two independent back gates (Fig. 2). The four corners of the map show the extremes of the four doping configurations available with two gates (NN, PP, PN, and NP). The large current in the upper right corner, the NN configuration, shows the superior contact the gold electrodes make to electrons. The off state of the device due to its band gap can be seen in the dark blue region in the center of the map, separating the NN region from the PP region. Along the diagonal line defined by $V_{bg} = V_{lg} = V_{rg}$, the device behaves as an ambipolar field effect transistor (Fig. 2c).

The current maps in Figs. 2a and b also show the current in the PN and NP configurations, where the gate voltages are adjusted to have opposite signs. For positive V_{ds} , current flows freely in the forward-biased PN region (upper-left corner) and is suppressed in the reverse-biased NP region (lower-right corner). When the bias is reversed this rectifying behavior is also reversed: current flows freely in the NP region and is suppressed in the PN region. Line cuts of this gate controlled rectifying behavior can be seen in Fig. 2d as a function of the voltage difference across the junction, $\Delta V_J = V_{lg} - V_{rg}$. We note a decrease in device performance between the datasets presented in Fig. 1 and Fig. 2, resulting in a substantially lower maximum current in Fig. 2.

The band gap of WSe₂ should lead to current suppression between each of the four doping configurations. This gap in conductance can be seen dividing NP from PP in the negative bias map and dividing PN from PP and weakly, PN from NN in the positive bias map. In negative bias, however, the NP and NN quadrants are connected by a conducting region. These gap filling states are most likely due to extrinsic disorder that creates a non-zero density of states within the band gap. Current through these states is thermally activated and can be eliminated by cooling the device to 200 K (see Supplementary Information).

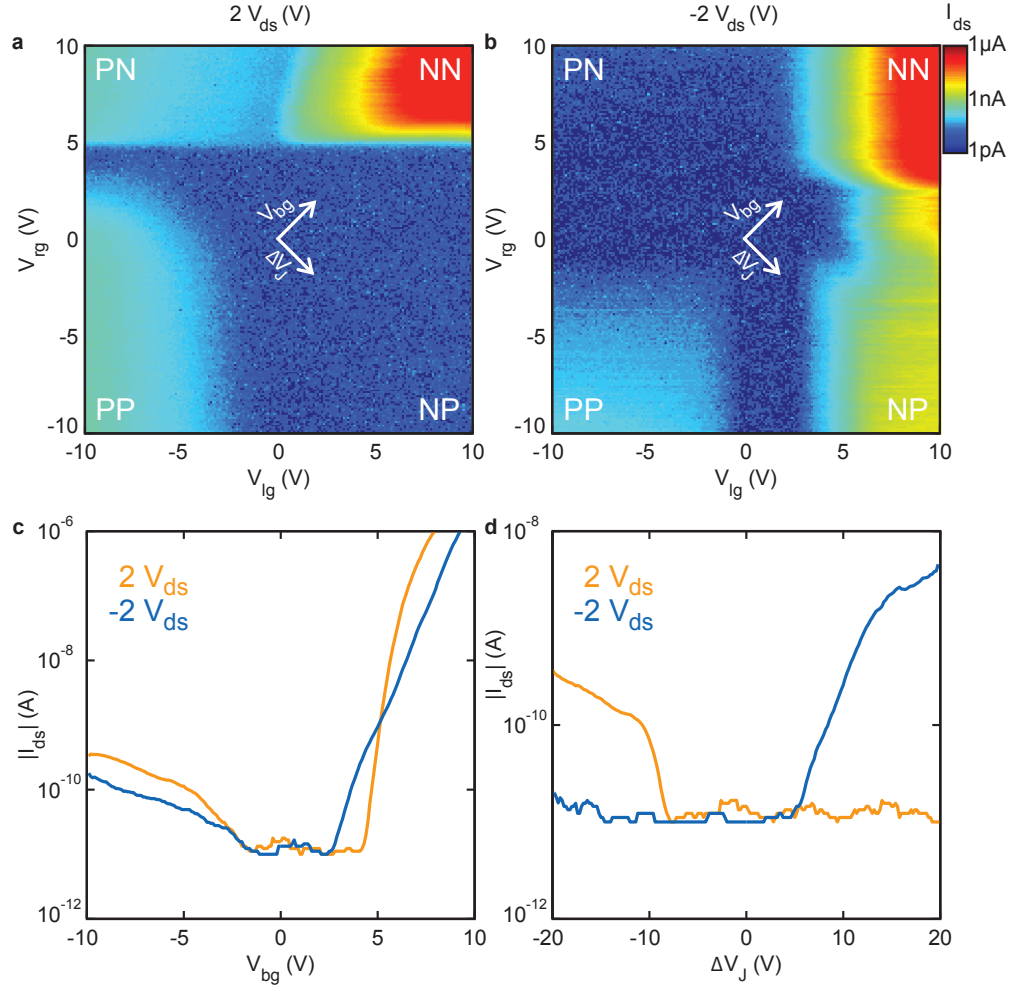


FIG. 2: **Current through the device in NN, PP, PN, and NP configurations.** **a, b**, Current magnitude through the device, $|I_{ds}|$, as the drain-source bias, V_{ds} , is held at 2 V (a) and -2 V (b) and the two back gates are varied independently. The color scale is logarithmic from 1 pA to 1 μ A. **c**, Current magnitude, $|I_{ds}|$, as both gates are swept together as one backgate, $V_{bg} = V_{lg} = V_{rg}$, at $V_{ds} = 2$ V (yellow curve) and -2 V (blue curve). These curves are characteristic of an ambipolar field-effect transistor. **d**, $|I_{ds}|$ as the two gates are swept with opposite polarity, showing the dependence on the voltage step across the junction, $\Delta V_J = V_{lg} - V_{rg}$. The current was measured at $V_{ds} = +2$ V (yellow curve) and -2 V (blue curve), demonstrating rectification of current in opposite directions for the PN ($\Delta V_J < 0$) and NP ($\Delta V_J > 0$) gate configurations.

Illuminating the device with laser light, we can probe the optoelectronic properties of monolayer WSe₂ PN diodes. Using scanning photocurrent microscopy (Fig. 3a), we measure current through the device as a laser spot ($\approx 2\mu\text{m}$ diameter) is scanned over the sample. A 532 nm diode laser, an 830 nm diode laser, and a band-pass filtered supercontinuum laser were used as the sources for these measurements.

With the gates set to the NP configuration ($V_{lg} = 10\text{ V}$, $V_{rg} = -10\text{ V}$), photons impinging on the junction create electron-hole pairs that are separated to opposite contacts by the electric field at the junction, generating a photocurrent. By scanning the beam (at $75\ \mu\text{W}$ from the 830 nm diode laser) over the sample and measuring drain current at $V_{ds} = 0$, we obtain a spatial map of the photoresponse of the NP junction (Fig. 3b). Calibrating the photocurrent map with a simultaneously acquired image of reflected light from the sample (see Supplementary Information), we overlay the positions of the contacts and gates to demonstrate that photocurrent arises when the light hits the NP junction. A line cut through the center of the photocurrent map is shown in Fig. 2c with the positions of the contacts and the junction illustrated for reference.

In the NP gate configuration and at relatively large V_{ds} , a substantial photocurrent is generated when the junction is illuminated with the 532 nm diode laser. The $I_{ds} - V_{ds}$ curves at laser powers from 0 to $10\ \mu\text{W}$ are shown in Fig. 3d. The photocurrent, $I_{ph} = I_{ds,light} - I_{ds,dark}$, at $-2\ V_{ds}$ and a linear fit of I_{ph} up to $8\ \mu\text{W}$ are shown in the inset. The slope from the fit gives a responsivity of $210\ \text{mA/W}$, which is comparable to commercial silicon photodetectors for green light. We note that dichalcogenide phototransistors can have even higher responsivities¹⁵, but this improved responsivity typically comes at the expense of detector response time.

In addition to photodetection, monolayer WSe₂ PN diodes are also capable of photovoltaic power generation. With the device in the NP configuration ($V_{lg} = 10\text{ V}$, $V_{rg} = -10\text{ V}$), current is measured as a function of V_{ds} for various laser powers from a 700 nm band-pass filtered supercontinuum laser (Fig. 4a). The short-circuit current, I_{sc} , is the zero-bias current through the illuminated device, which increases linearly with power up to at least $10\ \mu\text{W}$ (Fig. 4a inset). The power generated by the photovoltaic device, $P = I_{ds} \cdot V_{ds}$, is shown for laser powers 0-10 μW in Fig. 4b. The photovoltaic power generation also has a linear dependence on laser power with a conversion of $\sim 40\mu\text{W/W}$ (see Supplementary Information).

Varying the voltage difference across the junction ($\Delta V_J = V_{lg} - V_{rg}$) at different laser powers, we observe a saturation in the short circuit current when $\Delta V_J \sim \pm 10\text{ V}$ (Fig. 4c). The current

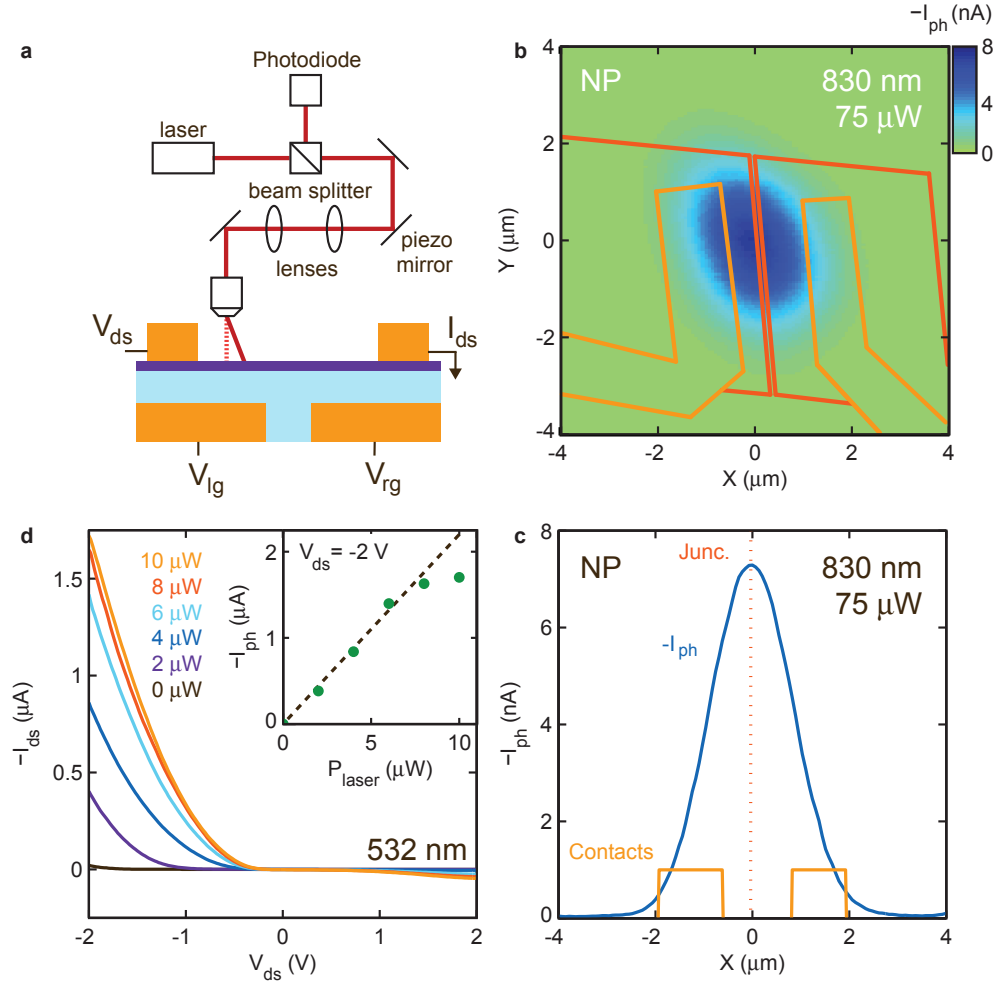


FIG. 3: **Photodetection.** **a**, Schematic of the scanning photocurrent microscopy setup and the device. The laser is focused onto the sample through a microscope objective at a position set by a piezo-controlled mirror. As the laser is scanned over the sample, photocurrent is recorded simultaneously with reflected laser power measured by a photodiode. **b**, Photocurrent, I_{ph} , as a function of laser position (830 nm diode laser at 75 μW), with the device in the NP configuration ($V_{lg} = 10$ V, $V_{rg} = -10$ V) and $V_{sd} = 0$ V. The peak in current corresponds to the location of the PN junction. Outlines of the contacts and gates are overlaid on the current map based on the reflected image (see Supplementary Information). **c**, Line cut from **b** at $Y=0$. Outlines of the contacts and the position of the junction are show in orange and yellow based on the reflected power image. **d**, I_{ds} - V_{ds} characteristics at different laser powers from 0 to 10 μW from a 532 nm diode laser with the device in the NP configuration. Inset: Plot of I_{ph} (green dots) at $V_{ds} = -2$ V as a function of laser power. A linear fit (black dashed line) to I_{ph} for powers from 0 to 8 μW gives a responsivity of 210 mA/W.

is higher for the NP configuration than for PN due to an asymmetry in the contact resistance that developed between the left and right contacts. We also note that the photocurrent due to the photovoltaic effect in these WSe₂ diodes is approximately an order of magnitude larger than photothermoelectric currents observed at the contacts of a monolayer MoS₂ field-effect transistor³¹.

To measure the spectral response of the photocurrent in the NP configuration, we measure I_{ds} as the wavelength of a supercontinuum source is scanned with a monochromator. To quantify the efficiency with which our device converts light into current at a particular wavelength, we extracted the external quantum efficiency, $\text{EQE} = (I_{sc}/P)(hc/e\lambda)$, as a function of wavelength, λ , at constant laser power, P (see Supplementary Information), with the constants h , c , and e , the Planck constant, speed of light, and electron charge, respectively. We observe three peaks in the spectrally resolved photocurrent at 755, 591, and 522 nm (Fig. 4d), corresponding to energies of 1.64, 2.10, and 2.38 eV, respectively, with a maximum EQE of 0.2% at 522 nm. These energies match well with the values predicted⁸ and experimentally observed via photoluminescence,⁵ differential reflectance,¹⁹ and optical absorption spectroscopy³² for the A, B, and A' transitions of monolayer WSe₂, as depicted in the band diagram in the inset to Fig. 4d.

Finally, we measure the electroluminescence spectrum of a second monolayer WSe₂ PN diode (Fig. 4d). To improve hole injection into the device, this device was fabricated with Pd instead of Au in contact with the p-type region of the WSe₂. With the device in the PN configuration, $V_{ds} = 2$ V and $I_{ds} = 100$ nA, the device behaves as a light-emitting diode (LED). The emitted light has a spectral peak at 752 nm, which corresponds with the direct gap exciton transition seen in the photocurrent spectrum (Fig. 4d). Light emission and a peak at ~ 750 nm can also be seen in the NP configuration ($V_{ds} = -2$ V and $I_{ds} = 4$ nA). No emission is seen in either the NN ($V_{ds} = 2$ V and $I_{ds} = 300$ nA) or PP ($V_{ds} = 2$ V and $I_{ds} = 500$ nA) configurations, confirming that the gate-defined PN junction generates the electroluminescence.

Based on the performance of the devices presented here, we anticipate a prominent role for diodes and optoelectronic devices based on monolayer dichalcogenide PN diodes, particularly taking into account the three-atom thickness and low optical absorption of monolayer WSe₂ (refs. 32,33). In addition, improved contact to the dichalcogenide, particularly for holes, should dramatically improve device performance. Finally, the device geometry could be optimized to significantly enhance photoresponse. In the split gate geometry studied here, the active region of the device is only a narrow line confined near the gap between the gates, so only a fraction of the incident

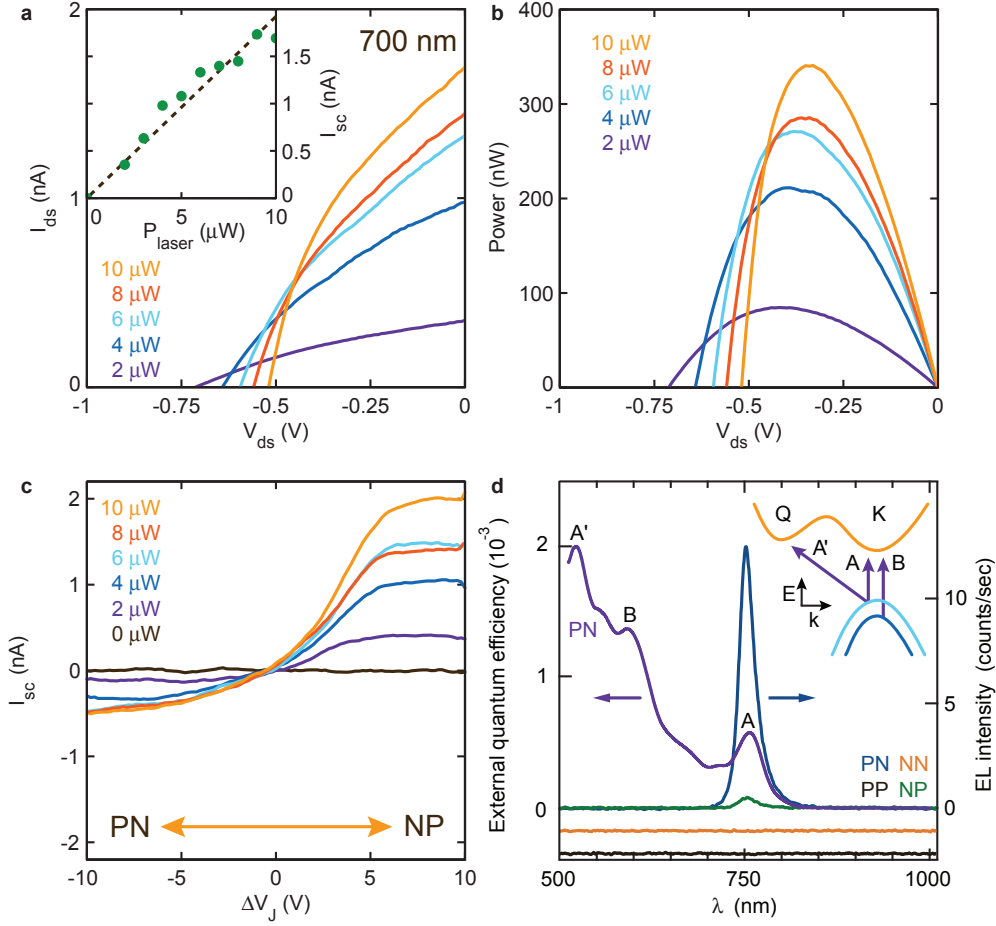


FIG. 4: **Photovoltaic response and light emission.** **a**, I_{ds} as a function of V_{ds} in the NP configuration ($V_{lg} = 10$ V, $V_{rg} = -10$ V) for laser powers from 2 to 10 μ W from a 700 nm band-pass filtered supercontinuum laser. Positive I_{ds} and negative V_{ds} in this regime reflects photovoltaic power generation. Inset: Short circuit current, I_{sc} (green dots), at $V_{ds} = 0$ versus laser power with a linear fit (black dashed line). **b**, Power, $P = I_{ds} \cdot V_{ds}$, produced by the device as a function of V_{ds} for different incident laser powers, calculated from the data in **a**. **c**, I_{sc} as a function of the voltage difference across the junction, ΔV_J , for different laser powers at $V_{ds} = 0$. I_{sc} is nearly linear with power up to 10 μ W in the NP configuration, but it saturates in the PN configuration beyond 6 μ W. As a function of gate voltage, the current saturates in both configurations for $\Delta V_J \sim \pm 10$ V. **d**, Left axis: External quantum efficiency as a function of wavelength at a constant laser power of 2 μ W. Peaks in the external quantum efficiency correspond to exciton transitions A, B, and A', as labeled. Right axis: Electroluminescence (EL) intensity at $V_{sd} = 2$ V in the PN, NN, and PP configurations and at $V_{sd} = -2$ V in the NP configuration. NN and PP traces are offset vertically for clarity. Inset: Diagram of the band structure around the K and Q points, with arrows indicating the lowest energy exciton transitions for monolayer WSe₂. The data in this figure were measured from device D1 except for the EL data. The EL data came from a second monolayer WSe₂ device with one Au and one Pd contact.

power from the laser spot contributes to photocurrent generation. We expect that a vertical junction structure based on transfer-aligned exfoliated flakes²⁴ or large-area dichalcogenides grown by chemical vapor deposition³² could increase responsivity and external quantum efficiency by more than an order of magnitude.

In conclusion, we have demonstrated electrically tunable PN diodes based solely on monolayer WSe₂. These diodes strongly rectify current, in a direction selectable by the voltage settings of the two gates controlling the device. Both the PN and NP configurations have diode ideality factors of $n = 1.9$ and a rectification factor of 10^5 . When laser light is incident on the junction, these diodes produce a large photocurrent with a responsivity of 210 mA/W at high bias. At low bias, the diodes generate power via the photovoltaic effect, with a peak external quantum efficiency of 0.2% at 522 nm. The spectral response of the photocurrent from visible to near infrared wavelengths showed peaks corresponding to the three lowest excitonic transitions expected for monolayer WSe₂. Finally, these devices can also function as light-emitting diodes with an electroluminescence peak at 752 nm. These PN junction diodes demonstrate the potential of monolayer WSe₂, in addition to other direct gap semiconducting dichalcogenides, for novel electronic and optoelectronic applications. As device quality improves, they also lay the foundation for more fundamental quantum transport experiments³⁴.

Note added: During the final preparation of this manuscript we became aware of similar work on PN diodes in monolayer WSe₂.³⁵

Acknowledgements

We acknowledge experimental assistance from Kamphol Akkaravarawong, Trond Andersen, Nathaniel Gabor, Qian Lu, Qiong Ma, and Javier Sanchez-Yamagishi and discussions with Patrick Brown. This work has been primarily funded by ONR Young Investigator Award N00014-13-1-0610, and partly by the ONR GATE MURI and a Packard Fellowship. This work made use of the MRSEC Shared Experimental Facilities supported by NSF under award No. DMR-0819762 and of Harvard's CNS, supported by NSF under Grant ECS-0335765.

Author contributions

B.W.H.B., H.O.H.C., and Y.Y. fabricated the samples, B.W.H.B., H.O.H.C., and Y. Y. performed the measurements, and all authors analyzed the data and co-wrote the paper.

Additional information

Supplementary information is available in the online version of the paper. Correspondence and requests for materials should be addressed to P.J-H. (pjarillo@mit.edu).

-
- ¹ S. Bertolazzi, J. Brivio, and A. Kis, *ACS Nano* **5**, 9703 (2011).
 - ² K. F. Mak, C. Lee, J. Hone, J. Shan, and T. F. Heinz, *Phys. Rev. Lett.* **105**, 136805 (2010).
 - ³ S. Chuang, R. Kapadia, H. Fang, T. C. Chang, W.-C. Yen, Y.-L. Chueh, and A. Javey, *Applied Physics Letters* **102**, 242101 (2013).
 - ⁴ K. S. Novoselov, D. Jiang, T. Booth, V. V. Khotkevich, S. M. Morozov, and A. K. Geim, *Proc. Natl. Acad. Sci. U. S. A.* **102**, 10451 (2005).
 - ⁵ W. Zhao, Z. Ghorannevis, L. Chu, M. Toh, C. Kloc, P.-H. Tan, and G. Eda, *ACS Nano* **7**, 791 (2013).
 - ⁶ A. K. Geim and I. V. Grigorieva, *Nature* **499**, 419 (2013).
 - ⁷ J. Wilson and A. Yoffe, *Advances in Physics* **18**, 193 (1969).
 - ⁸ Y. Ding, Y. Wang, J. Ni, L. Shi, S. Shi, and W. Tang, *Physica B: Condensed Matter* **406**, 2254 (2011).
 - ⁹ V. Podzorov, M. E. Gershenson, C. Kloc, R. Zeis, and E. Bucher, *Applied Physics Letters* **84**, 3301 (2004).
 - ¹⁰ B. Radisavljevic and A. Kis, *Nature Materials* **12**, 815 (2013).
 - ¹¹ B. W. H. Baugher, H. O. H. Churchill, Y. Yang, and P. Jarillo-Herrero, *Nano Letters* **13**, 4212 (2013).
 - ¹² Y. J. Zhang, J. T. Ye, Y. Yomogida, T. Takenobu, and Y. Iwasa, *Nano Letters* **13**, 3023 (2013).
 - ¹³ H. Wang, L. Yu, Y.-H. Lee, Y. Shi, A. Hsu, M. L. Chin, L.-J. Li, M. Dubey, J. Kong, and T. Palacios, *Nano Letters* **12**, 4674 (2012).
 - ¹⁴ Z. Yin, H. Li, H. Li, L. Jiang, Y. Shi, Y. Sun, G. Lu, Q. Zhang, X. Chen, and H. Zhang, *ACS Nano* **6**, 74 (2012).
 - ¹⁵ O. Lopez-Sanchez, D. Lembke, M. Kayci, A. Radenovic, and A. Kis, *Nature Nanotechnology* **8**, 497 (2013).
 - ¹⁶ A. Splendiani, L. Sun, Y. Zhang, T. Li, J. Kim, C.-Y. Chim, G. Galli, and F. Wang, *Nano Letters* **10**, 1271 (2010).

- ¹⁷ R. S. Sundaram, M. Engel, A. Lombardo, R. Krupke, A. C. Ferrari, P. Avouris, and M. Steiner, *Nano Letters* **13**, 1416 (2013).
- ¹⁸ Y. Ye, Z. Ye, M. Gharghi, H. Zhu, M. Zhao, X. Yin, and X. Zhang (2013), arXiv:1305.4235.
- ¹⁹ H. Zeng, G.-B. Liu, J. Dai, Y. Yan, B. Zhu, R. He, L. Xie, S. Xu, X. Chen, W. Yao, et al., *Sci. Rep.* **3** (2013).
- ²⁰ K. F. Mak, K. He, J. Shan, and T. F. Heinz, *Nature Nanotechnology* **7**, 494 (2012).
- ²¹ G. Sallen, L. Bouet, X. Marie, G. Wang, C. R. Zhu, W. P. Han, Y. Lu, P. H. Tan, T. Amand, B. L. Liu, et al., *Phys. Rev. B* **86**, 081301 (2012).
- ²² A. M. Jones, H. Yu, N. Ghimire, S. Wu, G. Aivazian, J. S. Ross, B. Zhao, J. Yan, D. Mandrus, and D. Xiao, *Nature Nanotechnology* **8**, 634 (2013).
- ²³ R. Spah, U. Elrod, M. Luxsteiner, E. Bucher, and S. Wagner, *Applied Physics Letters* **43**, 79 (1983).
- ²⁴ C. R. Dean, A. F. Young, I. Meric, C. Lee, L. Wang, S. Sorgenfrei, K. Watanabe, T. Taniguchi, P. Kim, K. L. Shepard, et al., *Nat Nano* **5**, 722 (2010).
- ²⁵ P. J. Zomer, S. P. Dash, N. Tombros, and B. J. van Wees, *Applied Physics Letters* **99**, 232104 (2011).
- ²⁶ M. M. Benameur, B. Radisavljevic, J. S. Hron, S. Sahoo, H. Berger, and A. Kis, *Nanotechnology* **22**, 125706 (2011).
- ²⁷ B. Radisavljevic, A. Radenovic, J. Brivio, V. Giacometti, and A. Kis, *Nature Nanotechnology* **6**, 147 (2011).
- ²⁸ T. Banwell and A. Jayakumar, *Electronics Letters* **36**, 291 (2000).
- ²⁹ C.-T. Sah, R. N. Noyce, and W. Shockley, *Proceedings of the IRE* **45**, 1228 (1957).
- ³⁰ J. Lambert, *Acta Helvetica, Physico-mathematico-anatomico-botanico-medica* **3**, 128 (1758).
- ³¹ M. Buscema, M. Barkelid, V. Zwiller, and H. van der Zant, *Nano Letters* **13**, 358 (2013).
- ³² J.-K. Huang, J. Pu, C.-P. Chuu, C.-L. Hsu, M.-H. Chiu, Z.-Y. Juang, Y.-H. Chang, W.-H. Chang, Y. Iwasa, and M.-Y. Chou, arXiv:1304.7365 (2013).
- ³³ M. Bernardi, M. Palummo, and J. C. Grossman, *Nano Letters* **13**, 3664 (2013).
- ³⁴ X. Li, F. Zhang, and Q. Niu, *Physical Review Letters* **110**, 066803 (2013).
- ³⁵ A. Pospischil, M. M. Furchi, and T. Mueller (2013), arXiv:1309.7492v1.